

# An In Situ Synchrotron X-Ray Diffraction Study on the Influence of Hydrogen on the Crystallization of Ge-Rich $\text{Ge}_2\text{Sb}_2\text{Te}_5$

Philipp Hans,\* Cristian Mocuta, Marie-Ingrid Richard, Daniel Benoit, Philippe Boivin, Yannick Le-Friec, Roberto Simola, and Olivier Thomas

To passivate Si –  $\text{SiO}_2$  dangling bonds, metal–oxide–semiconductor field-effect transistor devices are usually treated with hydrogen. Herein, the effects of such a treatment on the crystallization behavior on N-doped, Ge-rich  $\text{Ge}_2\text{Sb}_2\text{Te}_5$  phase-change materials for memory applications are investigated using synchrotron X-ray diffraction (XRD) in situ during heat treatment. Uniform thin films, and laterally confined, metallized ones (simulating devices of different complexity) of initially amorphous N-doped GGST are investigated. The specimens are heated up to 450–500 °C at a rate of 2 °C/min. Some of the specimens are treated with H/D; the equivalent untreated specimen is investigated for each of them. Crystallization onsets are estimated by quantification of the crystallized quantity during material transformation from the XRD patterns. In thin films, the hydrogen treatment results in lowered crystallization temperatures of the emerging cubic, metastable  $\text{Ge}_2\text{Sb}_2\text{Te}_5$  phase. Its trigonal, thermodynamically stable polymorph always forms, but its crystallization temperature is unchanged. Patterned and metallized samples show less differences, are strongly textured, and no trigonal phase is observed. It is shown that certain questions might only be answered at large-scale facilities where high energy photons are available at high flux, allowing data acquisition during the annealing process with a temperature resolution sufficient for a fine description of the sample transformation.

## 1. Introduction


Phase-change materials (PCMs) have the property to reversibly switch through controlled (local) heating, between an amorphous and a crystalline phase. These two phases exhibit a large contrast in both electrical and optical properties. This makes PCMs very

interesting for the digital, nonvolatile storage of information. Indeed, they have been used for a long time in Rewritable Compact Disks<sup>[1]</sup> (where writing is performed by laser heating and reading by low power laser optical reflectivity measurement). More recently, it has been realized that writing and reading can be performed using an electrical current, and thus opening the path to phase-change random access memories (PCRAM). Thereby, PCMs constitute a very promising alternative to Flash technology, which is reaching fundamental limits. One of their key advantages is their speed (in the tens of ns) and their scalability. As the energy consumption of PCMs scales with size, a promising solution is the (lateral) geometrical confinement of the memory points in insulating matrices.<sup>[2–5]</sup>

To reach crystallization temperatures above 350 °C, which is needed for automotive applications,<sup>[6]</sup> STMicroelectronics has developed a composition optimized Ge-rich material within the Ge–Sb–Te ternary system, GGST. GGST is a tailored variation

of  $\text{Ge}_2\text{Sb}_2\text{Te}_5$ , one of the most studied PCMs (very often in thin films; in the literature, it is often simply called GST). This composition optimized Ge-rich material within the Ge–Sb–Te ternary system will be named GGST herein. Previous studies on 50 nm thin films have shown<sup>[7]</sup> that the crystallization proceeds in two steps with Ge crystallization preceding the crystallization

P. Hans, O. Thomas  
IM2NP UMR 7334  
Aix-Marseille Université  
CNRS  
Campus de St-Jérôme, 13397 Marseille Cedex 20, France  
E-mail: philipp.hans@im2np.fr

 The ORCID identification number(s) for the author(s) of this article can be found under <https://doi.org/10.1002/pssr.202100658>.

© 2022 The Authors. physica status solidi (RRL) Rapid Research Letters published by Wiley-VCH GmbH. This is an open access article under the terms of the Creative Commons Attribution License, which permits use, distribution and reproduction in any medium, provided the original work is properly cited.

DOI: 10.1002/pssr.202100658

C. Mocuta  
Synchrotron SOLEIL  
l'Orme des Merisiers  
Saint-Aubin-BP 48, 91192 Gif-sur-Yvette, France

M.-I. Richard  
ID01/ESRF  
The European Synchrotron  
71 rue des Martyrs, 38043 Grenoble, France

D. Benoit, Y. Le-Friec  
STMicroelectronics  
850 rue Jean Monnet, 38920 Crolles, France

P. Boivin, R. Simola  
STMicroelectronics  
190 Ave Coq, 13106 Rousset, France

of cubic, metastable  $\text{Ge}_2\text{Sb}_2\text{Te}_5$ ).<sup>[1]</sup> Another variable that allows tuning the properties of GST-based PCMs is N-doping. An increased N-content reduces mechanical stresses related to crystallization, and strongly reduces Ge crystallization, probably by the formation of a  $\text{GeN}_x$  compound.<sup>[7–11]</sup>

It is state of the art to reduce the density of interface states in metal–oxide–semiconductor (MOS) transistors, resulting in, e.g., neutralized Si –  $\text{SiO}_2$  dangling bonds, by hydrogen treatment in devices.<sup>[12]</sup> As H is known to be a very fast diffuser, it is expected that it will reach the PCM. Thus, for embedded PCM memories applications, it is crucial to assess the influence of the different process steps used in MOS technology and in particular the influence of hydrogen treatment on the product. In this work, we aimed at determining the influence of hydrogen treatment on the crystallization behavior in the N-doped Ge-rich Ge–Sb–Te alloy GGST. Some specimens were treated either with  $\text{H}_2$  or  $\text{D}_2$  but as they are chemically equivalent, it is generally spoken of hydrogen treatment.

To investigate PCMs, X-ray diffraction (XRD) has proved to be a valuable tool for the investigations of such materials. XRD is one of the few techniques that has the potential to nondestructively distinguish the crystalline from the noncrystalline state (and to determine the average atomic arrangement). Each crystalline phase scatters X-rays in specific angles, especially strong, which leads to multiple, systematic peaks (Bragg reflections) that can be analyzed, for example, in terms of: peak positions (can be assigned to a specific phase and lattice spacing  $d$ -values and lattice parameters can be calculated thereof to analyze, e.g., strain in the material), integrated peak intensities (are related to the amount of crystallized material and give information about phase change dynamics), or peak widths (e.g., one can derive an estimate from the full width at half maximum [FWHM] for average crystallite sizes). Such analyses can be sophisticated in arbitrary complexity. The unique features of synchrotron radiation and equipment (2D detectors), owing to strong penetration by radiation, high photon fluxes, and high count rates, provide a nondestructive way to probe a material at short acquisition times. This is especially important when it comes to the investigation of technical specimens that are embedded in absorbing matrices and

contain only small quantities of the PCM where synchrotron radiation even allows for in situ investigations.

## 2. Results and Discussion

In this work, first, a comparison of in situ XRD experiments during annealing of thin films is given. Then patterned and metallized samples are analyzed. Patterned and metallized samples are interesting subjects for investigation because in contrast to blanket films, they are much closer to application where the geometrical (lateral) confinement of the memory points (at ultimate dimensions typically 5 nm in extension) is a promising solution for PCM-based memories. **Table 1** gives an overview of the specimens that were investigated in the present study. They were subjected to heating ramps, first with  $10^\circ\text{C}/\text{min}$  up to  $180^\circ\text{C}$  (to reduce the total time of the experiment) and then at a rate of  $2^\circ\text{C}/\text{min}$  up to  $450$ – $500^\circ\text{C}$ , a temperature far above when crystallization (emergence of Bragg reflections) is first observed. XRD patterns were recorded in situ; methodological details are presented in the Experimental Section. **Figure 1** gives a sketch of the arrangement of layers in the thin film only samples. The structure of the patterned and metallized samples is too complex to be easily represented.

The blanket GGST thin films TFU and TFT (annealed under  $\text{H}_2$ ) appeared to be amorphous in their pristine state. **Figure 2** shows an XRD pattern that was recorded after in situ annealing. The experimentally accessible range is  $q = 1.7$  to  $q = 3.2 \text{ \AA}^{-1}$  with the used setup. Based on phase analysis, three possible phases were identified (literature values are given): cubic Ge (space group  $\text{Fd}3\text{m}$ ; lattice parameter  $a = 5.65735 \text{ \AA}$ ),<sup>[13]</sup> cubic  $\text{Ge}_2\text{Sb}_2\text{Te}_5$  ( $\text{Fm}-3\text{m}$ ;  $a = 6.0293 \text{ \AA}$ ; high density of defects),<sup>[1]</sup> and trigonal  $\text{Ge}_2\text{Sb}_2\text{Te}_5$  ( $\text{P}-3\text{m}1$ ;  $a = 4.2247 \text{ \AA}$ ,  $c = 17.2391 \text{ \AA}$ ).<sup>[1]</sup> The trigonal  $\text{Ge}_2\text{Sb}_2\text{Te}_5$  phase is the thermodynamically stable phase opposed to the cubic, metastable  $\text{Ge}_2\text{Sb}_2\text{Te}_5$  phase.<sup>[1]</sup> It seems remarkable that the peaks of the  $\text{Ge}_2\text{Sb}_2\text{Te}_5$  phases do not fit well to the experimental pattern. This is an indication for a structure in the thin film that is strained or strongly distorted by point defects. Crystallization was followed by monitoring the Ge 111, Ge 220, and cGST111 or cGST200 and tGST013 peaks. In this

**Table 1.** Overview of the four investigated specimens: TFU, thin film untreated; TFT, thin film treated (annealed under  $\text{H}_2$ ); PMU, patterned metallized untreated; PMT, patterned metallized treated (annealed under  $\text{D}_2$ ). All experiments have been conducted under  $\text{N}_2$ -atmosphere and each heating ramp was performed at  $2^\circ\text{C}/\text{min}$ . TFU was heated to  $500^\circ\text{C}$  where the  $\text{Ge}_2\text{Sb}_2\text{Te}_5$  reflections vanished. Then, TFT was heated only to  $450^\circ\text{C}$  to be able to record also the  $\text{Ge}_2\text{Sb}_2\text{Te}_5$ 's behavior upon cooling.

Name	Agent	$T_{\text{max}}$	Sample details
All specimens were prepared by sputtering layers on monocrystalline Si substrate			
Blanket thin films: 30 nm SiO <sub>2</sub> @ 380 °C; 75 nm Si <sub>N</sub> @ 380 °C; an experimental thin connecting layer of modified GGST composition 45 nm GGST (high N-content); 20 nm TiN; and 25 nm SiN @ 320 °C			
TFU	H	500 °C	TFT: passivation is achieved by introduction of H by the following procedure:
TFT		450 °C	1) deposition of SiO <sub>2</sub> by PECVD (920 nm, 275 °C). This layer contains H.
			2) 600 nm SiN at 320 °C. This layer is a diffusion barrier for H.
			3) Anneal 320 °C, 30 min under N <sub>2</sub> . This anneal is aimed at inducing H diffusion.
PMU	D	500 °C	Same stack as for TF but patterned (50 nm wide lines) and lower N-content. In these samples, a partial process has been applied: silicided active areas, W plugs, two metallization levels of Cu.
PMT		500 °C	These are thus samples very close to a final product with embedded PCM memories.
			PMT: passivation is achieved by annealing at 350 °C for 2 h in D <sub>2</sub> at high pressure.

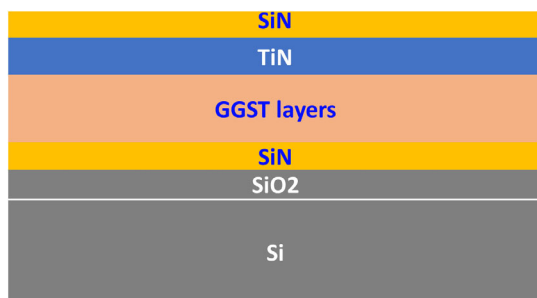


**Figure 1.** Sketch of the arrangement of the layers in the thin film only samples (TFT, TFU).

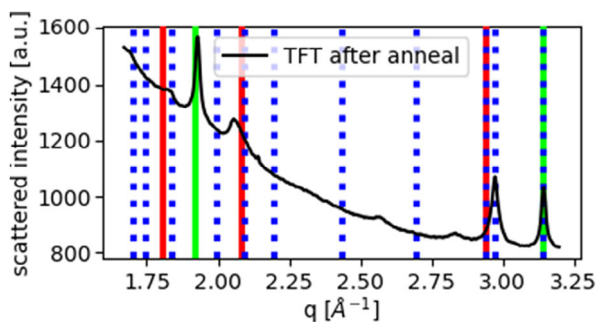


**Figure 2.** Possible (known) emerging phases in the GGST system in TFT after annealing: Ge (green), metastable cubic  $\text{Ge}_2\text{Sb}_2\text{Te}_5$  (red), and thermodynamically stable trigonal  $\text{Ge}_2\text{Sb}_2\text{Te}_5$  (blue). The peak positions were derived from crystal structure descriptions taken from [1] where an investigation of powdered annealed thin films is reported.

work, a multippeak refinement using Voigt functions after determination of a suited background was performed (see details in Experimental Section). The peak areas (integrated intensities) give information about the quantity of a phase; changes can be interpreted as a change of crystallized fraction and reveal information about phase change dynamics. Forming ratios of integrated peak intensities within one phase allows one to estimate texture. FWHMs can be used to coarsely estimate of crystallite sizes as a deduced quantity by calculating  $2\pi/\text{FWHM}$ .

**Figure 3** shows the emergence of a shoulder (tGST013) at smaller diffraction angles to the cGST200 reflection. This result first supports the previous findings of the formation of a mixture of crystalline Ge and a cubic  $\text{Ge}_2\text{Sb}_2\text{Te}_5$  phase. It furthermore shows the in fact known but commonly not quantified phenomenon of the trigonal  $\text{Ge}_2\text{Sb}_2\text{Te}_5$  phase emerging besides the Ge and cubic  $\text{Ge}_2\text{Sb}_2\text{Te}_5$  phases. With the applied fitting method, it was possible to account for the formation of the trigonal phase. Its formation is always observed in all thin film specimens.

Based on the fitting results, **Figure 4** and **5** show the evolution of the integrated intensities in the TFU versus the TFT (annealed under  $\text{H}_2$ ) sample. The integrated peak intensities (areas) of the Ge 111, Ge 220, cGST 111, cGST 200, and t-GST 013 reflections are plotted against the temperature in **Figure 4**. **Figure 5** shows the evolution of the approximate, average crystallite sizes for the corresponding peaks. **Figure 6** provides a comparison for the crystallization onset temperatures ( $T_x$ ) for each reflection.

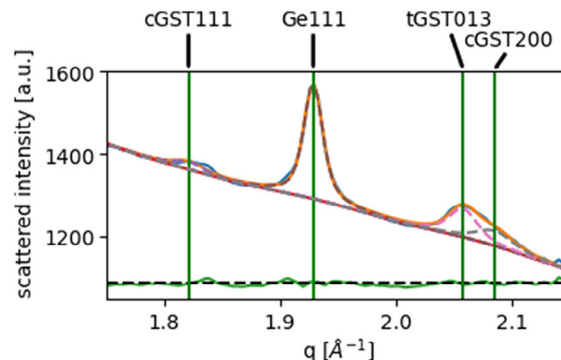


**Figure 3.** Double peak fit to explain the shoulder on the left side of the assumed cGST 200 reflection by means of a tGST 013 reflection. The green curve is the difference between simulation and experimental curve that was shifted by an offset and oscillates around 0.

Starting with sample TFU, it is remarkable that the integrated intensity of the Ge 111 reflection evolves in four stages (I, II, III, IV). Stage I (325–350 °C) is characterized by a sharp onset of the curve, indicating a rapid crystallization of Ge. Stage II (350–375 °C) is characterized by a slowdown of the process and is followed by stage III (375–385 °C) where another acceleration is observed, indicating a rapid crystallization. The process slows down again in stage IV (beginning at 385 °C). The corresponding approximate crystallite sizes do not rapidly change until approximately 450 °C which indicates primarily Ge nucleation and crystallite growth only sets in above this temperature in stage IV. The evolution of the Ge 220 reflection appears to follow a similar trend as the Ge 111 one, except that stage I is not present. Crystallization appears to go on even after arriving at a relatively high temperature. A tentative explanation for this steady increase in the Ge integrated intensity might be that it becomes more and more difficult to crystallize the remaining free Ge fraction, possibly because of a slow diffusion in the surrounding  $\text{Ge}_2\text{Sb}_2\text{Te}_5$  matrix. Also, very surprisingly, the onset temperatures for the Ge 111 and Ge 220 peak appearance are not the same. This is an indicator of evolving texture in the specimen and will be discussed below.

The cGST 111 reflection intensity emerges delayed in comparison to Ge but exhibits a similar behavior with a first fast initial stage I (starting at around 380 °C), a stage II at a slower rate, and finally in III an increase. The cGST 200 and tGST 013 reflections become visible at the same  $T_x$  as the cGST 111 reflection. It is characterized by a fast starting stage I that is followed by a stage II at slower rate. Stage III shows a steady increase then. From the comparison of the cGST 200 and tGST 013 reflections, one can conclude that the crystallization of the tGST occurs at the same temperature as cGST but it appears to evolve at a slower rate. Stage III (above 440 °C) seems associated with  $c \rightarrow t$  transformation in  $\text{Ge}_2\text{Sb}_2\text{Te}_5$ , i.e., the growth of the trigonal phase appears to be at the expense of the cubic phase.

In contrast to TFU, the evolution of Ge in TFT (annealed under  $\text{H}_2$ ) looks different. While the Ge 111 reflection appears at the same  $T_x$  as in TFU, the trend is different and it appears that only two stages exist. Grain growth sets in earlier and appears to be present from the onset of crystallization. One of

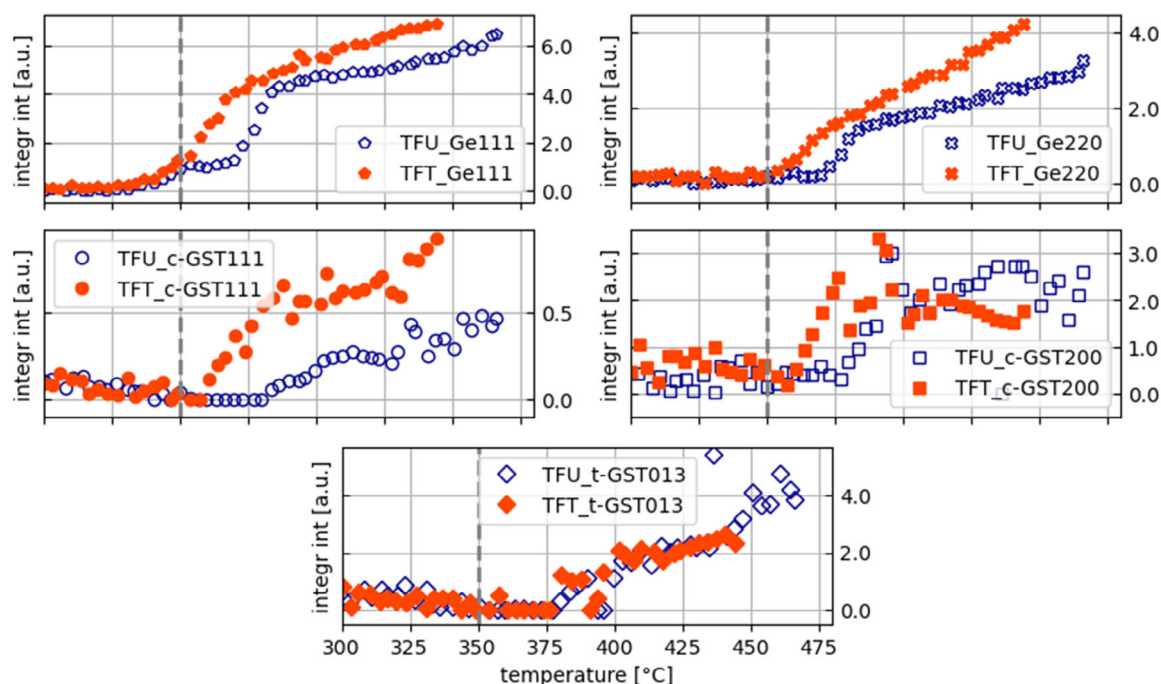


**Figure 4.** TFU versus TFT (annealed under  $H_2$ ): the top graph gives a comparison over coarsely estimated temperature onset for each reflection. Below is a comparison of the evolution of the integrated intensities of the Ge 111, Ge 220, cGST 111, cGST 200, and tGST 013 reflections.

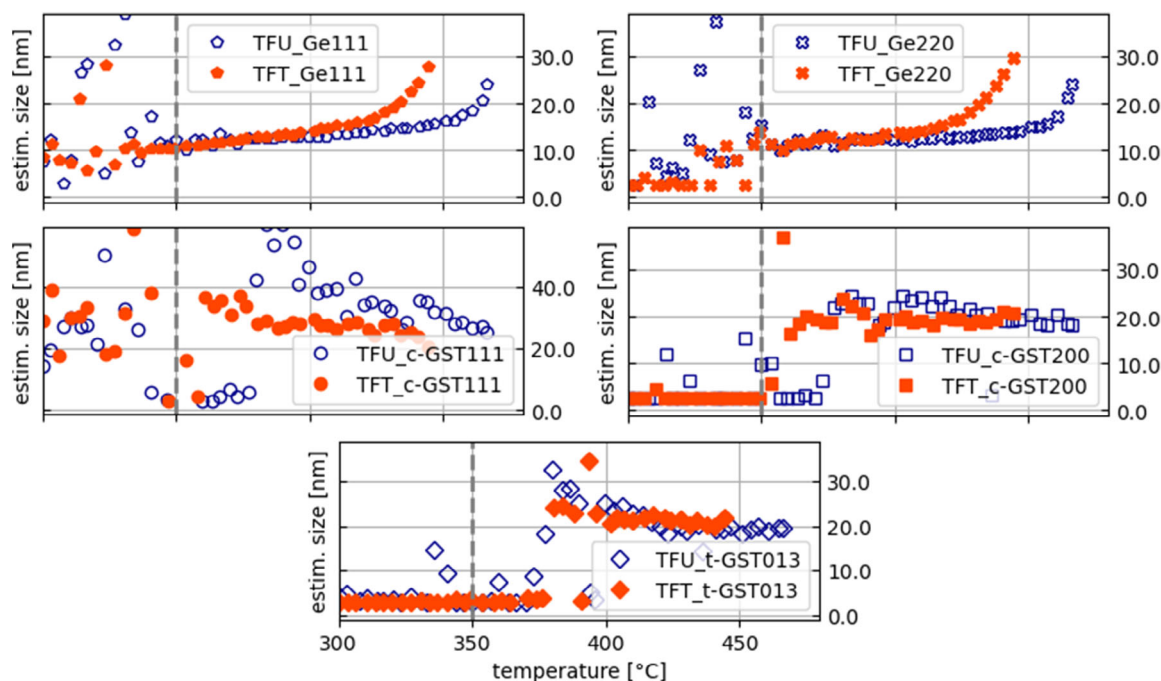


**Figure 5.** TFU versus TFT (annealed under  $H_2$ ): comparison of the evolution of the approximate, average crystallite sizes derived from the Ge 111, Ge 220, cGST 111, cGST 200, and tGST 013 reflections.

the most important findings is the reduced onset for cGST crystallization in the hydrogen-treated sample. Both the cGST 111 and cGST 200 reflections again appear simultaneously but at

a lower temperature than the tGST 013 reflection. The integrated peak intensity of the cGST 111 reflection shows a slightly increasing trend with temperature in both samples and is more



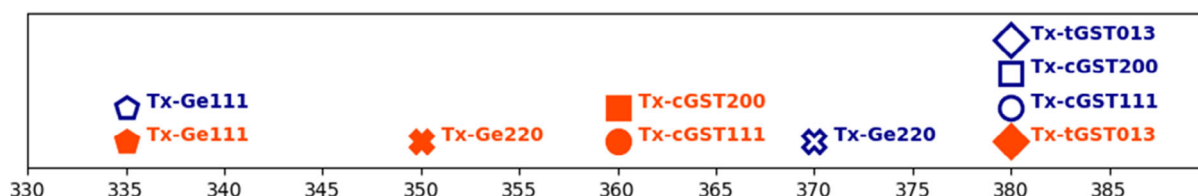


**Figure 6.** TFU versus TFT (annealed under  $H_2$ ): comparison of the crystallization onsets that were derived from the Ge 111, Ge 220, cGST 111, cGST 200, and tGST 013 reflections.

pronounced in TFT (annealed under  $H_2$ ). As a rationalization, one might note that the angular region of this peak has a highly nonuniform background and might be prone to parasitic scattering and evolution of texture.

In both TFT and TFU, the GST crystallite sizes seem to saturate after a short initial phase of growth. It appears worthy to point out that sizes between 30 and 40 Å are quickly approached (a value that is reached for the Ge only slowly).

In the previous figure it was seen that the Ge 111 and Ge 220 reflections do not appear simultaneously in neither TFU nor TFT (annealed under  $H_2$ ). This breaks the simple relationship between integrated intensity and amount of crystallized materials. The most striking case occurs at the beginning of crystallization when Ge 111 is present but Ge 220 is undetectable. **Figure 7** gives a comparison of the evolution of the ratio of the Ge220/Ge111 reflections in TFU and TFT (annealed under  $H_2$ ). In both specimens the ratio is changing, meaning a change in texture. It is only noted at this point that if a very strong texture was present (close to epitaxial), the XRD would, in principle, not allow to detect more than one Bragg reflection with an area detector at a fixed geometry as it was used in the experiments. Any assumption about the texture in the material would need experimental validation.

It is interesting to look at the sum of the Ge 111 and Ge 220 reflection intensities to see how the material behaves. It is more reliable than the individual peaks, i.e., less sensitive to texture changes. In order to get an estimate of the total amount of crystallized  $Ge_2Sb_2Te_5$ , it is also worth looking at the sum of the integrated cGST 200 and tGST 013 reflection intensities, representing the two polymorphic phases, which should represent the total amount of crystallized  $Ge_2Sb_2Te_5$ . **Figure 8** gives such a comparison: the summed peak areas of the Ge 111 and Ge 220 reflections (left) and the summed areas of the overlapping

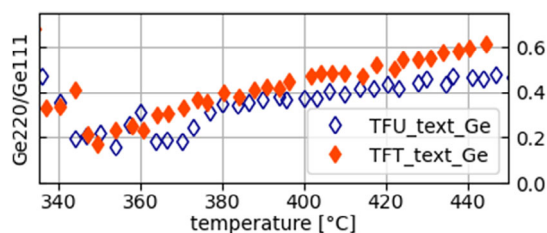


**Figure 7.** Comparison of textures of Ge calculated from the ratio Ge 220: Ge 111. The ratio is increasing which means that the crystallographic texture changes with temperature. This could be one explanation for the steady increase of the crystallized fraction of Ge as estimated from the Ge 111 peak area.

cGST 200 and tGST 013 reflections (right). It can be seen that the crystallization of Ge in TFU happens slower and at higher temperature while the total amount of  $Ge_2Sb_2Te_5$  is increasing. From the characteristic XRD peaks, it appears that the crystallization of the Ge in TFU is continuously increasing, while the  $Ge_2Sb_2Te_5$  one is reaching a plateau. This is another remarkable influence of hydrogen treatment on the crystallization behavior of GGST.

The investigation of patterned samples (PMU and PMT) is much more difficult than the one from thin films because of the considerable reduction in the volume of scattering material. As can be seen from **Figure 9**, the diffracted intensity is, as expected, much smaller. The GST in samples PMU and PMT (annealed under  $D_2$ ) appears to exhibit considerable texture because the cGST200 reflection is quasi missing.

**Figure 10** gives a comparison of the evolution of the integrated intensities in PMU and PMT (annealed under  $D_2$ ). **Figure 11** gives a comparison of the evolution of the corresponding estimated crystallite sizes. One notes that for both the Ge and the cGST phase some crystallized material is present in the initial state. This is probably a consequence of the thermal budget used for the different metallization steps. As a consequence, the crystallization observed during our in situ experiments is strongly influenced by the occurrence of preexisting crystallites.

From the evolutions shown in **Figure 6**, it can be concluded that samples PMU and PMT (annealed under  $D_2$ ) share a very similar behavior: the  $T_x$  for Ge and cGST are very close to one another and the increase in the quantity of crystalline material and crystallite size as a function of temperature shares the same trends. As there is some crystallized material from the start, it is probable that part of these trends can be attributed to grain growth. There is, however, a clear increase in the integrated intensities which shows that a significant amount of PCM was not yet crystallized during the metallization process.

In summary, the following trends have been observed from the described in situ synchrotron XRD study: 1) In all the investigated samples, the formation of crystalline Ge precedes the one of  $Ge_2Sb_2Te_5$ . The crystallite orientation of Ge appears to be evolving with temperature. 2) tGST is formed simultaneously to cGST in untreated thin films. 3) Hydrogen treatment leads to a reduction of the cGST crystallization onset in thin films. It appears approximately 25°C (at 2°C/min) before tGST starts to crystallize. A hypothesis for why hydrogen treatment decreases the crystallization temperature would be that H, which is known to be a very fast diffuser, easily penetrates the GGST material and segregates at the surface of the  $Ge_2Sb_2Te_5$  nuclei. This might

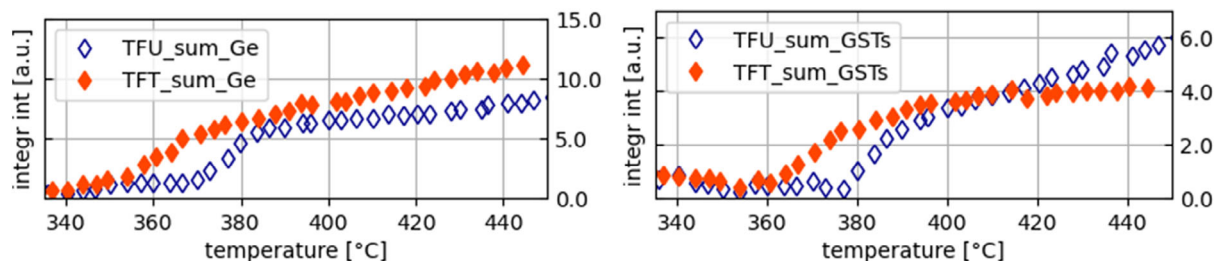


**Figure 8.** (left) Sums of the integrated intensities of the Ge 111 and Ge 200 diffraction peaks and (right) sums of the areas of the cGST 200 and tGST 013 reflections in thin film samples versus temperature.

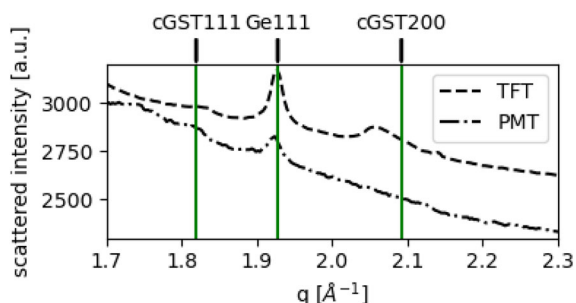


**Figure 9.** Comparison between the diffraction patterns of TFT (annealed under  $H_2$ ) and PMT (annealed under  $D_2$ ) after annealing. Besides reduced scattering intensities, the patterned and metallized samples PMU and PMT (annealed under  $D_2$ ) appear to be strongly textured because the cGST200/tGST013 reflection is missing. For this reason, only the cGST111 peak can be considered for comparisons.

lead to a decrease of the crystalline–amorphous interface energy and thus decreases the energy barrier for nucleation. 4) It was possible to give an approximate quantification of the  $Ge_2Sb_2Te_5$  phases and in both thin film samples cGST appears

to transform into tGST. From the interpretation of the evolution of the sums of the Ge 111 and Ge 220, and the cGST 200 and tGST 013 reflection areas, it was observed that the crystallization of Ge in TFU is slower than in TFT (annealed under  $H_2$ ) while the total amount of  $Ge_2Sb_2Te_5$  is increasing. Oppositely, in TFT Ge appears to increase crystallizing while  $Ge_2Sb_2Te_5$  appears to level off. 5) In patterned and metallized specimens a) Ge and  $Ge_2Sb_2Te_5$  preexist (explainable by thermal pretreatments) and b) the onsets of crystallization are shifted for both phases to much higher temperatures (approximately  $60 \pm 10^\circ C$ ). As that T-shift is not observed in patterned samples with no metallization ([7]) and hydrogen treatment appears to lower the crystallization onsets, the conclusion is drawn that preprocessing steps or stress induced by the metallization layers might be the reason for the strong shift of  $T_x$ .

### 3. Conclusions

To conclude, we have performed in situ XRD experiments on a range of specimens (thin films and patterned thin films partly with additional metallization layers) to elucidate the influence of hydrogen on the crystallization onsets of Ge and  $Ge_2Sb_2Te_5$  in Ge-rich

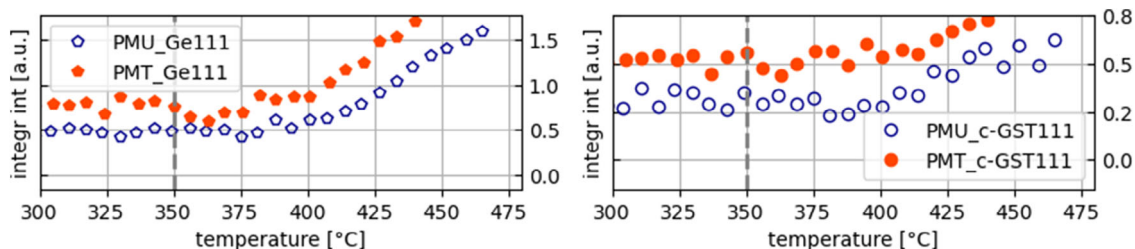


**Figure 10.** PMU versus PMT (annealed under  $D_2$ ): comparison of the evolution of the integrated intensities of the cGST 111 and Ge 111 reflections.

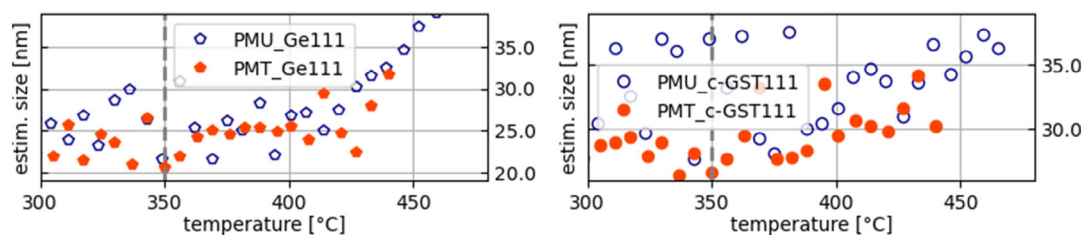


**Figure 11.** PMU versus PMT (annealed under  $D_2$ ): comparison of the evolution of the approximate, average crystallite sizes derived from the cGST 111 and Ge 111 reflections.

Ge–Sb–Te alloys, a promising material for PCRAMs. As deposited, capped GGST thin films appear amorphous from the XRD patterns. After crystallization a mixture of Ge and cubic, metastable  $\text{Ge}_2\text{Sb}_2\text{Te}_5$  is observed in all specimens as expected. It is remarkable that in thin films the thermodynamically stable trigonal  $\text{Ge}_2\text{Sb}_2\text{Te}_5$  emerges with no or little delay to cubic  $\text{Ge}_2\text{Sb}_2\text{Te}_5$  phase. It could be observed that the effect of hydrogen or deuterium treatment, respectively, leads to a lowering of the  $T_x$  of both Ge and  $\text{Ge}_2\text{Sb}_2\text{Te}_5$ . This effect is reduced or non-existent in the preprocessed, patterned samples. One interesting finding is that those patterned samples exhibit around 60 °C elevated crystallization onsets which was not expected. In the course of the heat treatment neither phase appears to ever fully crystallize. The authors find it worthy to mention that some of the specimens investigated here are very close to final products (several metallization layers on top), so that the presented findings can be an important result for the manufacturing and application processes. The study furthermore demonstrates the unique capability of synchrotron XRD to probe and characterize the PCM in its “real device” environment.

## 4. Experimental Section

**Data acquisition and reduction:** The series of annealing experiments was performed and followed by in situ XRD at the DiffAbs beamline of SOLEIL synchrotron. The specimens were annealed under  $\text{N}_2$  atmosphere up to 450–500 °C at a rate of 2 °C/min using an Anton Paar heating stage that was mounted on the six-circle diffractometer (Kappa geometry). The beam size was  $205 \times 255 \mu\text{m}^2$  ( $\text{FWHM} = V \times H$ ). The XRD patterns were recorded in vertical scattering geometry at a fixed incident angle  $\omega = 10^\circ$  (yielding a beam footprint on the specimen surface:  $1473 \times 255 \mu\text{m}^2$ ) using an XPAD S140 hybrid pixel array X-ray detector.<sup>[14,15]</sup> An incident photon energy  $E = 18 \text{ keV}$  was chosen in order to measure a large reciprocal space region with one single detector position. With diffraction angles investigated close to  $20^\circ$ , the direction of the scattering vector is approximately normal to the specimen surface. The 1D diffraction patterns (scattered intensity as a function of the diffraction angle  $2\theta$ ) were obtained by azimuthal integration and by applying geometrical, polarization, and flat-field corrections.<sup>[16]</sup> Then, a conversion of the diffraction angles to the X-ray wavelength independent  $q$ -scale with  $q = 4\pi \sin(\theta)/\lambda$  was performed.

**Data analysis:** To each peak of interest, a Voigt profile<sup>[17–19]</sup> was fitted. A Voigt function is defined as the convolution of a Gaussian function with a Lorentzian function (functions centered at  $q = 0$  are shown below). The solution is possible only numerically but efficient and accurate algorithms to calculate the Voigt profile exist.<sup>[20]</sup>

$$V(q; \sigma, \gamma) = (G * L)(q) = \int_{-\infty}^{\infty} G(q'; \sigma) L(q - q'; \gamma) dq' \quad (1)$$

with  $G(q; \sigma)$  and  $L(q; \gamma)$  as Gaussian profile and Lorentzian profiles

$$G(q; \sigma) = \frac{e^{-q^2/(2\sigma^2)}}{\sigma\sqrt{2\pi}} \quad \text{and} \quad L(q; \gamma) = \frac{\gamma}{\pi(q^2 + \gamma^2)} \quad (2)$$

and

$$1 = \int_{-\infty}^{\infty} V(q; \sigma, \gamma) dq \quad \text{so that} \quad A = A \int_{-\infty}^{\infty} V(q; \sigma, \gamma) dq \quad (3)$$

In the above equations,  $q$  is the shift from the line center,  $\sigma$  corresponds to the standard deviation of the Gaussian distribution,  $\gamma$  is half the FWHM of the Lorentz distribution, and  $A$  is the area of the

Voigt function. In the limiting cases of  $\sigma = 0$  or  $\gamma = 0$   $V(q; \sigma, \gamma)$  simplifies to  $L(q; \gamma)$  or  $G(q; \sigma)$ .

Analyses of the data were performed by a custom config file-based software solution written in the Python3 scripting language<sup>[21]</sup> and might be discussed in more detail in a dedicated publication or on <https://github.com/phlpphns>. Particular attention was given to find and handle also very weak diffraction peaks on a strong background. The procedure coarsely consists of three parts: 1) baseline estimation (the python pybaselines module was used) applying a Baseline Estimation And Denoising with Sparsity (BEADS)<sup>[22]</sup> algorithm for baseline identification, 2) manual identification of peaks and experimental range of interest to configure the general boundary conditions of the high throughput fitting, and 3) fitting the peaks of interest in defined intervals by means of a differential evolutionary approach with the lmfit library.<sup>[23]</sup> Other non-standard libraries were numpy,<sup>[24]</sup> matplotlib,<sup>[25]</sup> pandas,<sup>[26]</sup> and scipy.<sup>[27]</sup> Theoretical peak positions were obtained from crystallographic information files with the VESTA software.<sup>[28]</sup>

## Acknowledgements

The authors would like to thank SOLEIL Synchrotron for allocating beamtime on DiffAbs beamline. Ph. Joly (Synchrotron SOLEIL, DiffAbs) is thanked for technical support. IPCEI/Nano 2022 program is acknowledged for partial funding of this work. The authors thank Christophe Guichet for help with data acquisition.

## Conflict of Interest

The authors declare no conflict of interest.

## Author Contributions

P.H. designed and implemented the overall data analysis procedure and data interpretation. P.H. drafted the manuscript and data interpretation. P.H. and O.T. mutually refined manuscript and data interpretation. C.M., C.G., M.I.R., and O.T. helped with collecting data. C.M. performed the reduction of 2D detector images to 1D patterns. D.B. and Y.L.F. prepared specimens. P.B. and R.S. were part of the experimental planning, discussions, and support. All authors read and approved the final version of the manuscript.

## Data Availability Statement

The data that support the findings of this study are available from the corresponding author upon reasonable request.

## Keywords

chalcogenides, crystallization, data storage, in situ synchrotron X-ray diffraction, phase-change materials

Received: December 28, 2021

Revised: February 7, 2022

Published online: March 1, 2022

[1] T. Matsunaga, N. Yamada, Y. Kubota, *Acta Crystallogr. Sect. B* **2004**, 60, 685.

[2] H.-S. P. Wong, S. Raoux, S. Kim, J. Liang, J. P. Reifenberg, B. Rajendran, M. Asheghi, K. E. Goodson, *Proc. of the IEEE* **2010**, 98, 2201.

- [3] R. F. Freitas, W. W. Wilcke, *IBM J. Res. Dev.* **2008**, 52, 439.
- [4] G. W. Burr, B. N. Kurdi, J. C. Scott, C. H. Lam, K. Gopalakrishnan, R. S. Shenoy, *IBM J. Res. Dev.* **2008**, 52, 449.
- [5] D. J. Wouters, R. Waser, M. Wuttig, *Proc. of the IEEE* **2015**, 103, 1274.
- [6] P. Zuliani, E. Palumbo, M. Borghi, G. Dalla Libera, R. Annunziata, *Solid-State Electron.* **2015**, 111 27.
- [7] O. Thomas, C. Mocuta, M. Putero, M.-I. Richard, P. Boivin, F. Arnaud, *Microelectron. Eng.* **2021**, 244, 111573.
- [8] A. Fantini, V. Sousa, L. Perniola, E. Gourvest, J. Bastien, S. Maitrejean, S. Braga, N. Pashkov, A. Bastard, B. Hyot, A. Roule, A. Persico, H. Feldis, C. Jahan, J. Nodin, D. Blachier, A. Toffoli, G. Reimbold, F. Fillot, F. Pierre, R. Annunziata, D. Benshael, P. Mazoyer, C. Vallée, T. Billon, J. Hazart, B. De Salvo, F. Boulanger, *2010 International Electron Devices Meeting*. **2010** 29.1.1.
- [9] R. Fallica, E. Varesi, L. Fumagalli, S. Spadoni, M. Longo, C. Wiemer, *phys. status solidi (RRL) – Rapid Res. Lett.* **2013**, 7, 1107.
- [10] T. Nirschl, J. Philipp, T. Happ, G. Burr, B. Rajendran, M.-H. Lee, A. Schrott, M. Yang, M. Breitwisch, C.-F. Chen, E. Joseph, M. Lamorey, R. Cheek, S.-H. Chen, S. Zaidi, S. Raoux, Y. Chen, Y. Zhu, R. Bergmann, H.-L. Lung, C. Lam, *2007 IEEE International Electron Devices Meeting* **2007** 461.
- [11] Y. Yin, H. Zhang, S. Hosaka, Y. Liu, Q. Yu **2013**, 46, 505311.
- [12] H. Takahashi, H. Yamada-Kaneta, *Appl. Surf. Sci.* **2003**, 216, 347, proc. of the Fourth Inter. Symp. on the Control of Semiconductor Interfaces Karuizawa, Japan, October 21-25, 2002.
- [13] R. W. G. Wyckoff, *Crystal Structures*, 1, second edn, Interscience Publishers, New York, NY **1963**.
- [14] S. Basolo, J.-F. Berar, N. Boudet, P. Breugnon, B. Caillot, J.-C. Clemens, P. Delpierre, B. Dinkespiller, I. Koudobine, C. Meessen, M. Menouni, C. Mouget, P. Pangaud, R. Potheau, E. Vigeolas, *IEEE Trans. Nucl. Sci.* **2005**, 52, 1994.
- [15] P. Pangaud, S. Basolo, N. Boudet, J.-F. Berar, B. Chantepie, J.-C. Clemens, P. Delpierre, B. Dinkespiller, K. Medjoubi, S. Hustache, M. Menouni, C. Morel, *Nucl. Instrum. Methods Phys. Res. Sect. A: Accelerators, Spectrometers, Detectors Associated Equipment* **2008**, 591, 159.
- [16] C. Mocuta, M.-I. Richard, J. Fouet, S. Stanesco, A. Barbier, C. Guichet, O. Thomas, S. Hustache, A. V. Zozulya, D. Thiaudière, *J. Appl. Crystallogr.* **2014**, 47, 482.
- [17] W. Voigt, Über das gesetz der intensitätsverteilung innerhalb der linien eines gasspektrums, **1912**, <https://publikationen.baw.de/de/003395768> (accessed: December 2021).
- [18] G. K. Wertheim, M. A. Butler, K. W. West, D. N. E. Buchanan, *Rev. Sci. Instrum.* **1974**, 45, 1369.
- [19] T. T. García, *Mon. Not. R. Astron. Soc.* **2006**, 369, 2025.
- [20] Z. Shippony, W. Read, *J. Quant. Spectros. Radiat. Transfer* **1993**, 50, 6 635.
- [21] G. Van Rossum, F. L. Drake, *Python 3 Reference Manual*, CreateSpace, Scotts Valley, CA, **2009**.
- [22] X. Ning, I. W. Selesnick, L. Duval, *Chemom. Intell. Lab. Syst.* **2014**, 139 156.
- [23] M. Newville, T. Stensitzki, D. B. Allen, A. Ingargiola, LMFIT: Non-Linear Least-Square Minimization and Curve-Fitting for Python, **2014**, <https://doi.org/10.5281/zenodo.11813> (accessed: December 2021).
- [24] C. R. Harris, K. J. Millman, S. J. van der Walt, R. Gommers, P. Virtanen, D. Cournapeau, E. Wieser, J. Taylor, S. Berg, N. J. Smith, R. Kern, M. Picus, S. Hoyer, M. H. van Kerkwijk, M. Brett, A. Haldane, J. Fernández del Río, M. Wiebe, P. Peterson, P. Gérard-Marchant, K. Sheppard, T. Reddy, W. Weckesser, H. Abbasi, C. Gohlke, T. E. Oliphant, *Nature* **2020**, 585, 357.
- [25] J. D. Hunter, *Comput. Sci. Eng.* **2007**, 9, 90.
- [26] W. McKinney, In *Proc. of the 9th Python in Science Conf.*, Austin, TX, **2010**, 445, 51.
- [27] P. Virtanen, R. Gommers, T. E. Oliphant, M. Haberland, T. Reddy, D. Cournapeau, E. Burovski, P. Peterson, W. Weckesser, J. Bright, S. J. van der Walt, M. Brett, J. Wilson, K. J. Millman, N. Mayorov, A. R. J. Nelson, E. Jones, R. Kern, E. Larson, C. J. Carey, *Nature Methods* **2020**, 17 261.
- [28] K. Momma, F. Izumi, *J. Appl. Crystallogr.* **2011**, 44, 1272.